Material-point erosion simulation of dynamic fragmentation of metals

B. Li [a], A. Pandolfi [b,*], M. Ortiz [a]

[a] *Graduate Aeronautical Laboratories, California Institute of Technology, Pasadena, CA 91125, USA*
[b] *Dipartimento di Ingegneria Civile ed Ambientale, Politecnico di Milano, 20133 Milano, Italy*

Received 9 November 2013
Received in revised form 4 March 2014
Available online 1 April 2014

1. Introduction

The present work is concerned with the validation of a material-point erosion scheme, termed *eigenerosion* (Schmidt et al., 2009; Pandolfi and Ortiz, 2012; Pandolfi et al., 2013), in applications involving detonation-driven fragmentation of metals. We base our validation assessment on the experiments of Campbell et al. (2007), in which a stainless steel spherical cap shell is pressurized by the detonation of explosive. Numerical simulations of dynamic fragmentation furnish an exacting test of frac-ture algorithms. Thus, under dynamic loading, cracks may develop stochastically, branch and reconnect, there-by drastically modifying the topology of the solid. Other challenges arise in connection with the development of extreme conditions of pressure, temperature, rate of deformation and energy density, often accompanied by phase transitions such as melting and vaporization. In regions of more moderate energy density, the material may still experience large deformations, strain localiza-tion, hydrodynamic instabilities, fracture and fragmenta-tion. In particular, explosive loading through the detonation of high explosives causes intense transient loading of the metal, following the arrival of pressure waves. Subsequent expansion and deformation of the metal leads to material tearing and crack opening (Campbell et al., 2007; Goto et al., 2008; Hiroe et al., 2008; Arnold and Rottenkolber, 2008). Theoretical inter-pretations of the dynamic fragmentation of rapidly expanding metal shells include the statistical theory of Mott (1947), the energy-based theories of Grady et al.(1984); Kipp et al. (1986), and others (Fressengeas and Molinari, 1994; Miller et al., 1999; Pandolfi et al., 1999; Repetto et al., 2000; Drugan, 2001; Guduru and Freund, 2002; Shenoy, 2003; Zhou et al., 2005; Zhang and Chen, 2009).

* Corresponding author. Address: Politecnico di Milano, Dipartimento di Ingegneria Civile ed Ambientale, Piazza Leonardo da Vinci 32, 20133 Milano, Italy. Tel.: +39 02 23994217; fax:+39 02 23994300.

E-mail addresses: libo@caltech.edu (B. Li), anna.pandolfi@polimi.it (A. Pandolfi), ortiz@aero.caltech.edu (M. Ortiz).

Element erosion has been extensively used to simulate fracture in a number of areas of application, including terminal ballistics (Johnson and Stryk, 1987; Belytschko and Lin, 1987; Ortiz and Giannakopoulos, 1990; Johnson and User, 1990; Whirley and Hallquist, 1991; Borvik et al., 2008). However, some of these methods fail to converge or converge to the wrong limit (Negri, 2003). These pathologies can be eliminated by means of local averaging schemes (Negri, 2003; Schmidt et al., 2009). In the present work, we focus on a particular averaged-erosion scheme, termed *eigenerosion* (Schmidt et al., 2009; Pandolfi and Ortiz, 2012; Pandolfi et al., 2013). An appealing aspect of this scheme is that it has proven convergence properties (Schmidt et al., 2009), namely, the solutions converge to those of Griffith fracture in the limit of a vanishingly small mesh size. When combined with material-point methods, i. e., methods that sample the state of the material at discrete or *material points*, eigenerosion may be implemented as a material-point erosion scheme, i. e., the material-points can be either intact, in which case their behavior is governed by constitutive equations, or be completely failed —or eroded—and have no residual load bearing capacity. The implementation of the method is straightfor-ward (Pandolfi and Ortiz, 2012; Pandolfi et al., 2013) and applies to general situations, possibly involving complex three-dimensional fracture patterns such as branching and fragmentation.

We specifically consider eigenerosion in conjunction with the Optimal Transportation Meshfree (OTM) method of Li et al. (2010, 2012), which combines optimal transportation as a means of time discretization with max-ent mesh-free spatial interpolation Arroyo and Ortiz, 2006 and material-point sampling (cf., e. g., Sulsky et al., 1994). OTM is specially well-suited to the simulation of unconfined plastic flows and, as a material-point based method, it provides a convenient framework for the implementation of eigenerosion and other similar schemes. Another convenient feature of OTM, especially in the context of fragmentation, where fragments often undergo complex collision sequences before scattering, is that *seizing contact* is accounted for automatically simply as a result of cancelation of linear momentum between adjacent fragments (cf. Li et al., 2012; Sulsky et al., 1994).

The paper is organized as follows. In Section 2 we briefly review the relevant features of the OTM method and of the eigenerosion scheme that provide the basis for the simulations. In Section 3 we describe the computational model, including the modeling of the explosive action and the material model. In Section 4 we present the results of the numerical simulation and compare them with the experimental data. We conclude in Section 5 with a summary and some concluding remarks.

2. The numerical algorithm: OTM and eigenerosion

In this work, we evaluate the eigenerosion scheme in the particular framework of the Optimal Transportation Meshfree (OTM) method (Li et al., 2010). The OTM method is a meshfree updated Lagrangian numerical scheme that combines concepts from Optimal Transportation theory (cf., e. g., Villani, 2003) with material-point sampling (cf., e. g., Sulsky et al., 1994) and local max-ent meshfree approximation (Arroyo and Ortiz, 2006). OTM has demonstrated excellent robustness, accuracy and convergence properties in applications involving dynamic deformation and failure of materials (Li et al., 2010, 2012) and, therefore, is ideally suited to the application of interest here.

The use of optimal transportation tools in OTM is intended as a means of formulating geometrically exact variational time-integration schemes for flow problems. In particular, the Benamou and Brenier (1999) differential formulation of optimal mass transportation problems and its connection to the Wasserstein distance (Jordan, 1998) is used to discretize the inertial action in time within a strictly variational framework. The resulting discretization may be regarded as the result of restricting the inertial action to mass measures concentrated on material points undergoing piecewise rectilinear motions. The optimal transportation variational framework results in: proper mass matrices and inertia forces in the presence of continuously varying spatial interpolation; geometrically exact mass transport and satisfaction of the continuity equation; and exact linear and angular momentum conservation. The total energy can also be exactly conserved, subject to solvability constraints, if time is taken as an independent generalized coordinate (Kane et al., 1999). In addition, the variational structure of OTM confers it robust convergence properties (Li et al., 2010, 2012).

Fields requiring differentiation, such as deformation and velocity fields, are interpolated from nodal values using max-ent shape functions (Arroyo and Ortiz, 2006). Maxent interpolation has the advantage of being mesh-free and entirely defined–essentially explicitly–by the current nodal-set positions. An additional key property of max-ent interpolation is that it possesses a Kronecker-del-ta property at the boundary, which enables the direct imposition of displacement boundary conditions. In calculations, the max-ent shape functions are reconstructed continuously 'on-the-fly' from the nodal set, thus overcoming the essential difficulties that arise in fixed grid-based numerical schemes like Lagrangian and Eulerian finite element methods.

The representational scheme underlying OTM is further illustrated in Fig. 1. The scheme employs two sets of points, namely, nodal points and material points. Material points result from the spatial approximation of the mass densities $\rho_{h,k}(x)$ by M point masses

$$\rho_{h,k}(x) = \sum_{p=1}^{M} m_p \delta(x - x_{p,k}), \tag{1}$$

where $x_{p,k}$ represents the position at time t_k of *material point* p, m_p is the mass of the material point and $\delta(x - x_{p,k})$ is the Dirac-delta distribution centered at $x_{p,k}$. Material points designate fix material points of the body, are convected by the deformation, carry a fixed volume and mass, serve the purpose of integration points for the calculation of the effective nodal forces and masses, and store all local state data. The spatial discretization is completed by approximating the deformation mapping as

$$\varphi_{h,k\to k+1}(x) = \sum_{a=1}^{N} x_{a,k+1} N_{a,k}(x), \tag{2}$$

where $x_{a,k}$ is the position at time t_k of *node a*, and $\mathcal{N}_{a,k}(x)$ are max-ent shape functions defined over the configura-tion at time t_k. The interpolation at a material point $x_{p,k}$ de-pends only on the nodes contained in a small local neighborhood $\mathcal{N}_{p,k}$ of the material point. The relative mo-tion between nodes and material points results in the need for frequent updates of the local neighborhoods, e.g., using range searches (Bentley and Friedman, 1979). This continuous reconstruction of the local neighborhoods has the effect of automatically reconnecting the material points and the nodal set, at *no cost of remapping* of the local states car-ried by the material points. This property of the method is particularly convenient for inelastic materials whose local material state often includes additional internal variable information.

Algorithm 1. OTM/eigenerosion time step

Require: Initial and final times for time step, t_k, t_{k+1}.
Require: Initial nodal coordinates, $x_k = \{x_{a,k},\ a = 1,\dots,N\}$.
Require: Initial material-point coordinates, $\{x_{p,k},\ p = 1,\dots,M\}$.
Require: Initial shape functions $\{\{N_{a,k}(x_{p,k}),\ a \in \mathcal{N}_{p,k}\},\ p = 1,\dots,M\}$.
Require: Ibid gradients $\{\{\nabla N_{a,k}(x_{p,k}),\ a \in \mathcal{N}_{p,k}\},\ p = 1,\dots,M\}$.
Require: Initial deformation gradients, $\{F_{p,k},\ p = 1,\dots,M\}$.
Require: Initial material state at all material points.
Require: Initial list of failed material points.
1: Compute mass matrix M_k, nodal forces f_k, accelerations $a_k = M_k^{-1} f_k$.
2: Update nodal coordinates: $x_{k+1} = x_k + (t_{k+1} - t_k)(v_k + \frac{1}{2}(t_{k+1} - t_{k-1})a_k)$.
3: Update nodal velocities: $v_{k+1} = (x_{k+1} - x_k)/(t_{k+1} - t_k)$.
4: Update material-point coords.: $x_{p,k+1} = \varphi_{k\to k+1}(x_{p,k}),\ p = 1,\dots,M$.
5: Update deformation grads.: $F_{p,k+1} = \nabla\varphi_{k\to k+1}(x_{p,k})F_{p,k},\ p = 1,\dots,M$.
6: Carry out constitutive updates at material points.
7: Compute energy-release rates $\{G_{p,k+1},\ p = 1,\dots,M\}$.
8: Add $\{p \,|\, G_{p,k+1} > G_c\}$ to failed material-point list.
9: Update local material-point neighborhoods $\mathcal{N}_{p,k+1},\ p = 1,\dots,M$.
10: Compute shape functions $\{N_{a,k+1}(x_{p,k+1}),\ a \in \mathcal{N}_{p,k+1}\},\ p = 1,\dots,M$.
11: Ibid gradients $\{\nabla N_{a,k+1}(x_{p,k+1}),\ a \in \mathcal{N}_{p,k+1}\},\ p = 1,\dots,M$.

The trajectories of the spatially discretized system follow from the discrete Hamilton's principle applied to the time-discretized action. The resulting time-integration scheme is listed in Algorithm 1. Conveniently, the OTM scheme can be solved forward explicitly. This forward solution has the usual structure of explicit time-integration and updated-Lagrangian schemes. In particular, all the finite kinematics of the motion, including the mass density and volume updates, are geometrically exact. In addition, the cancelation of linear momentum automatically accounts for dynamic contact interactions of the seizing type (Sulsky et al., 1994). Collisions may be efficiently detected by fast orthogonal range query algorithms such as kd-tree and cell searches. In comparison to the penalty method, Lagrangian multipliers or other meshfree contact algorithms (Li et al., 2001), the OTM method provides an efficient alternative for simulating complex collision sequences such as occur as a result from fragmentation during ballistic impact.

Finally, we briefly outline the material-point failure scheme used to simulate fracture and fragmentation phenomena in terminal ballistics calculations. Within the context of OTM calculations, fracture can be modeled simply by failing material points according to an energy-release criterion. When the material points are failed, they are neglected from the computation of stresses in the model, which approximates the presence of cracks. Following (Schmidt et al., 2009; Li et al., 2012; Pandolfi and Ortiz, 2012; Pandolfi et al., 2013) we compute the energy-release rate attendant to the failure of material point p as

$$G_{p,k+1} = \frac{C\epsilon}{m_{p,k+1}} \sum_{x_{q,k+1}\in B_\epsilon(x_{p,k+1})} m_q W_k(F_{q,k+1}), \tag{3}$$

where $B_\epsilon(x_{p,k+1})$ is the ball of radius ϵ centered at $x_{p,k+1}$, or *ϵ-neighborhood* of the material point, cf. Fig. 2,

$$m_{p,k+1} = \sum_{x_{q,k+1}\in B_\epsilon(x_{p,k+1})} m_q \tag{4}$$

is the mass of the ϵ-neighborhood, $W_k(F_{q,k+1})$ is the incremental free-energy density per unit mass in the sense of variational constitutive updates (Ortiz and Stainier, 1999) and C is a normalizing constant. The averaging radius ϵ defines a length scale intermediate between the discretization size and the macroscopic size of the bodies. The material point is failed when

$$G_{p,k+1} \geqslant G_c, \tag{5}$$

where G_c is a critical energy release rate that measures the material-specific energy required to create a fracture surface of unit area. In calculations, the failed material-point set is updated at every time step according to criterion (5), cf. Algorithm 1.

For linear elasticity, Schmidt et al. (2009) have shown that criterion (3) and (5) result in approximations that converge to Griffith fracture in the limit of an infinitely fine discretization. We note that averaging over an intermediate ϵ-neighborhood in order to compute the energy-release rate attendant to material-point failure, Eq. (3), is essential to convergence. Indeed, erosion schemes that estimate the energy-release rate based on the energy of a single material point suffer from mesh-dependency and may overestimate the toughness of the material (Negri, 2003).

We remark that there are no theoretical rules to select the size of the ϵ radius. In order to prove the convergence

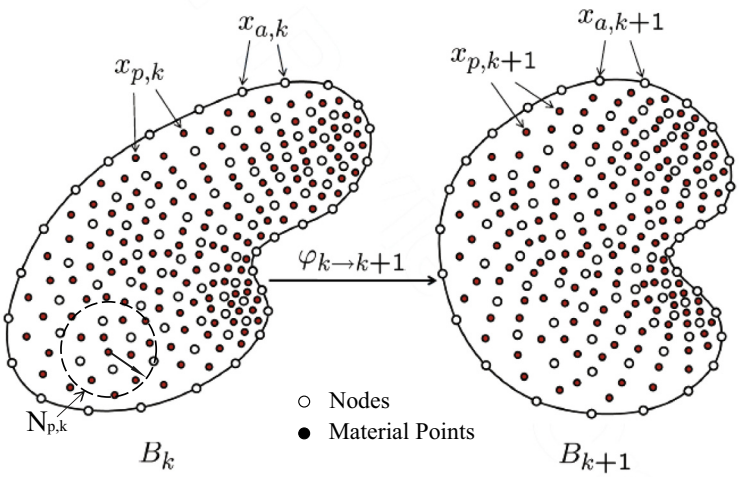

Fig. 1. Spatial discretization scheme used in the OTM method. The figure describes one step of the application of the method between times t_k and t_{k+1}. The open circles represent the nodal points and the full circles the material points. B_k and B_{k+1} are the configurations of the body at times t_k and t_{k+1}, respectively, and $\varphi_{k\to k+1}$ is the corresponding incremental deformation mapping. $N_{p,k}$ is the local neighborhood of material point $x_{p,k}$ that supports the local max-ent mesh-free interpolation.

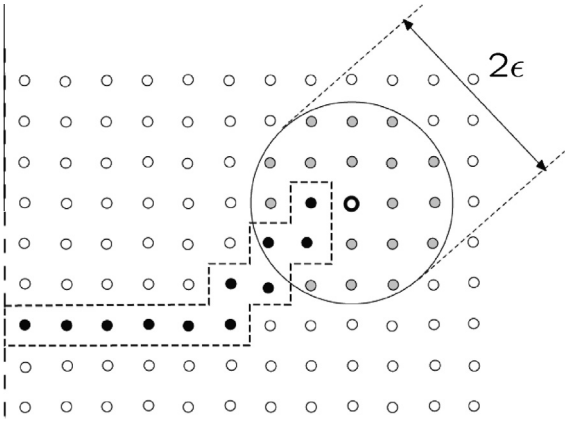

Fig. 2. (a) Visualization of the crack (black dots) as set of failed material points, and of the ϵ-neighborhood (grey dots) of the material point located at the crack tip (hollow dot).

of the method, ϵ is requested to go to zero with the mesh size h, although less rapidly. In practice, the definition of the ϵ radius requires some preliminary calculations on the given geometry.

We also observe that when a material point satisfies the erosion condition, its contribution to the internal force vector and to the material stiffness matrix is set to zero, but its contribution to the mass matrix is maintained. The mass of a material point is discarded only when an eroded material point is not connected to any nodes.

3. Application to explosively-driven spherical-cap tests

We apply the OTM method and eigenerosion scheme to the simulation of explosively driven dynamic fragmentation experiments on spherical-cap shells (Campbell et al., 2007). The experimental setup consists of a spherical cap machined from a rolled plate of 304L stainless steel loaded with 912.5 g of high energy explosive. The radius of curvature R of the spherical cap is 200 mm, the in plane diameter is 184 mm, and the thickness is 3 mm. Along the perimeter of the cap, a lip mates a supporting ring. A 20 mm thick layer of explosive with specific detonation energy 5.5 kJ/g is located on the back side of the shell, and the detonator is set in correspondence to the symmetry axis, see Fig. 3.

3.1. Explosive action

The simulation of the denotation is beyond the scope of the present study. Therefore the action of the explosive is described by means of an idealized pressure history applied to the back surface of the shell parameterized according to the experimental data reported in Campbell et al. (2007). In particular, the distribution of the peak pressure originated by the detonation is taken to be

$$p_{\text{peak}}(r) = P_{\max} \exp\left(-f\,\frac{r}{R_l}\right), \tag{6}$$

where r is the distance from the symmetry axis, $P_{\max}$ is the maximum pressure at the center of the shell, $R_l = 92$ mm is the in-plane radius and f is a decay coefficient. The peak pressure waves travel from the center of the shell to the edge in the time interval $T_{\max}$. The arrival time t_0 of the pressure wave front at the distance r is estimated through a linear interpolation as

$$t_0(r) = T_{\max}\,\frac{r}{R_l}. \tag{7}$$

The parameters $P_{\max} = 33.3$ GPa, $f = 1.745$, and $T_{\max} = 10.4$ μs have been chosen according to the data reported in Campbell et al. (2007). Finally, the variation of the pressure in time is assumed to be described by the modified Friedlander equation (Ortiz and Pandolfi, 2004) that reads

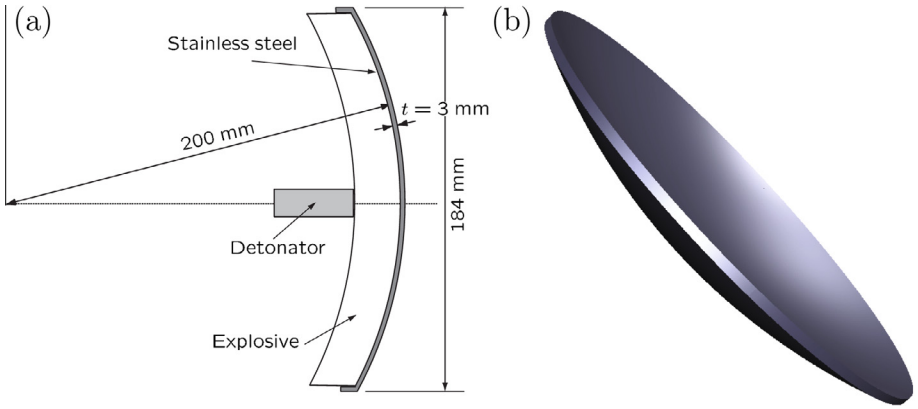

Fig. 3. (a) A schematic illustration of the experimental setup. The stainless material is located in the outer shell. The explosive is located in the concave part of the shell and the detonator is placed at the symmetry axis. (b) Geometry of the numerical model.

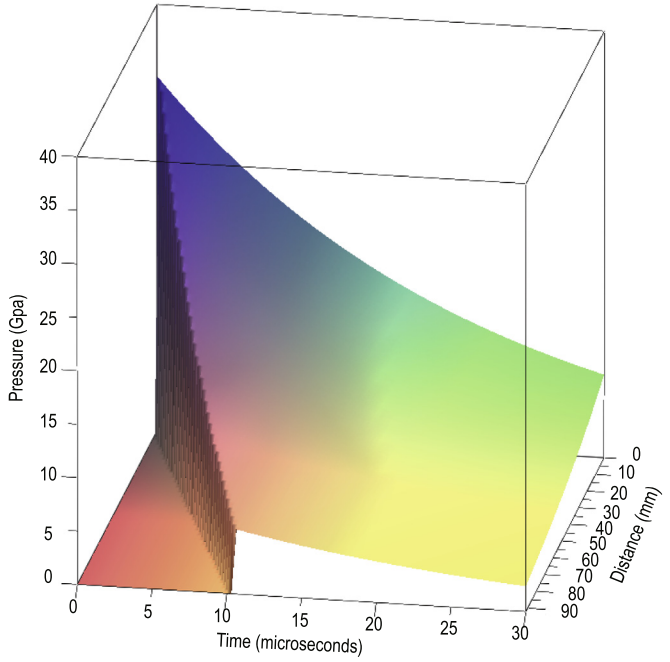

Fig. 4. Pressure boundary conditions as a function of space and time.

$$p(r,t) = \begin{cases} p_{\text{peak}}(r)\,\frac{T_p - t + t_0(r)}{T_p - t_0(r)}\exp\left(-c\,\frac{t}{T_p}\right), & \text{if} \quad t \geqslant t_0(r), \\ 0, & \text{otherwise.} \end{cases} \tag{8}$$

The duration time $T_p = 2500\mu s$ and the dimensionless decay coefficient $c = 120$ in (8) are interpolated from standard explosion tables (Kinney, 1962), using the actual yield factor λ of the explosion, i. e.,

$$\lambda = \left(\frac{W}{W_{\text{ref}}}\right)^{1/3} = 0.106 \tag{9}$$

where $W_{\text{ref}} = 4.184$ GJ is the reference energy released by 1 t TNT equivalent and $W = 5049$ kJ is the total energy of the explosion, i. e., the specific detonation energy times the explosive weight. Fig. 4 depicts the variation in time of the distribution of the pressure along a radius of the shell.

3.2. Material model

In order to model the extensive plastic deformation observed in the 304L stainless steel employed in the experiments (Campbell et al., 2007), we adopt a J_2-viscoplasticity model with power-law hardening, rate-sensitivity, and thermal softening (cf., e. g., Camacho and Ortiz, 1997; Yadav et al., 2001; Li et al., 2012). Of particular concern is the modeling of the rate-sensitivity

of the 304L stainless steel at the high-strain rates prevalent in the experiment. Thus, transmission electron microscopy observations of the recovered fragments reveal the presence of a non negligible amount of martensite phase, cf. Fig. 16 of Campbell et al. (2007). The transition from austenite to martensite takes places at strain rates of the order of $10^4\ s^{-1}$ (Klopp et al., 1985; Clifton and Klopp, 1985; Tong et al., 1992) and a single power rate-sensitivity law is inadequate to describe the rate sensitivity of both phases. In order to overcome this limitation, we resort to the two-phase rate-sensitivity model (Marusich and Ortiz, 1995)

$$\dot{\epsilon}^p = \dot{\epsilon}_0^p \left(\frac{\sigma - \sigma_c(\epsilon^p, T)}{\sigma_0} \right)^{m_1} \quad \text{if} \quad \dot{\epsilon}^p \leqslant \dot{\epsilon}_t, \tag{10a}$$

$$\dot{\epsilon}^p = \left(\frac{\dot{\epsilon}_0^p}{\dot{\epsilon}_t} \right)^{m_2/m_1 - 1} \left(\frac{\sigma - \sigma_c(\epsilon^p, T)}{\sigma_0} \right)^{m_2} \quad \text{if} \quad \dot{\epsilon}^p > \dot{\epsilon}_t, \tag{10b}$$

where $\dot{\epsilon}_0^p$ is the reference effective plastic-strain rate, σ is the effective stress, ϵ^p is the effective plastic strain, T is the absolute temperature, σ_0 is the reference stress, m_1 and m_2 are the low and the high strain rate sensitivity exponent, respectively, and $\dot{\epsilon}_t$ is the strain rate that acts as threshold between the two regimes. The critical stress σ_c for plastic yielding is taken to be of the form

$$\sigma_c(\epsilon^p, T) = Y(T) \left[1 + \left(\frac{\epsilon^p}{\epsilon_0^p} \right)^{1/n} \right], \tag{11}$$

where $Y(T)$ is the yield stress, ϵ_0^p is the reference effective plastic strain, and n is the hardening exponent. The yield stress additionally undergoes thermal softening according to the relation

$$Y(T) = \sigma_y \left(1 - \frac{T - T_0}{T_m - T_0} \right)^l, \tag{12}$$

where σ_y is the yield stress at the reference temperature, $T_0 = 298$ K and T_m are the reference and melting temperature respectively, and l is the thermal softening exponent.

The elastic response is assumed to be isotropic and quadratic in the elastic logarithmic strains, with elastic coefficients linearly dependent on the temperature and vanishing at the melting temperature. The volumetric response of the material is governed by the Mie-Gruneisen equation of state.

Finally, in calculations we assume adiabatic heating and we take the sole source of heat to be the plastic working of the material. The rate of heating per unit undeformed volume is computed as

$$S = \beta \dot{W}^p, \tag{13}$$

where $\beta = 0.9$ is the Taylor-Quinney coefficient and $\dot{W}^p$ is the plastic power per unit undeformed volume. We solve the resulting coupled thermo-mechanical problem by a staggered procedure (Lemonds and Needleman, 1986). In the attendant mechanical isothermal step, the constitutive equations are integrated in time by recourse to the variational constitutive updates of Ortiz and Stainier (1999).

The contact between fragments is assumed to be of the seizing type, corresponding to an infinite coefficient of friction. The parameters of the model, as reported in the literature (Campbell et al., 2007; Yadav et al., 2001), are collected in Table 1.

4. Numerical results and comparison to experiments

The computational model accounts for the spherical part of the shell cap only and omits the lip and the circumferential supports, see Fig. 5(a). The baseline discretization contains 182,969 nodes and 931,932 material points uniformly distributed on 12 layers across the thickness, Fig. 5b. Concurrent calculations were carried out in the Shared Heterogeneous Cluster (SHC), consisting of 1,156 AMD Opteron cores and an Infiniband connection, of Cal-tech's Center for Advanced Computing Research (CACR). The MPI parallel version of the three-dimensional OTM code executes 40 μs simulations of the explosion test on 512 cores in about 8 h of CPU time.

Sequential snapshots from the simulations at times 4.5, 9, 14 and 25 μs, respectively, are shown in Fig. 6. Colored contour levels refer to the von Mises stress. As may be seen from the figure, the simulation captures the significant phases of the experiment. The pressure exerted by the explosive on the back side of the shell induces plastic deformations that start to develop in the center and propagate circumferentially towards the free edge. The central zone is the first to experience fragmentation, Fig. 6a. Simultaneously with outward propagation of the plastic front, the center of the shell fractures progressively, eventually assuming a petal-like shape. Extensive erosion of material points, involving roughly 40% of the original mass of the shell cap, agrees with the observed pulverization of the steel, see Fig. 6b. Once the plastic strains have covered uniformly the entire cap, they start to localize along the meridians, in the process developing a periodic and symmetric structure, Fig. 6c. In the late stages of the simulation, the localized plastic strains develop into radial cracks, thereby resulting in elongated fragments of varying sizes, see Fig. 6d.

The distribution of the fragments at $t = 30$ μs is visualized in Fig. 7, which shows a snapshot of the spatial distribution of material points still connected to another material point. The non-eroded one-material point fragments are removed from the picture in order to better visualize the geometry of the larger fragments. After 30 μs from the beginning of the analysis, no further material point erosion is observed, and the fragments keep their size flying all around. Fig. 8 compares the experimental (Campbell et al., 2007) and numerical distributions of the

Table 1
Material properties for 304L stainless steel.

ρ kg/m^3	E GPa	ν	G_c N/m	σ_y MPa	n	m_1	m_2	ϵ_0^p	$\dot{\epsilon}^p$ 1/s	$\dot{\epsilon}_t$ 1/s	T_m K	l
8000	193	0.3	28,000	200	22	20	5	0.001	1	10,000	1777	1.17

(a) nodal set (b) material point set

Fig. 5. (a) Material point discretization of the spherical cap shell, consisting of 182,969 nodes and 931,932 material points. (b) View of a quarter of the shell cap, showing the layered structure of the material points across the cap thickness.

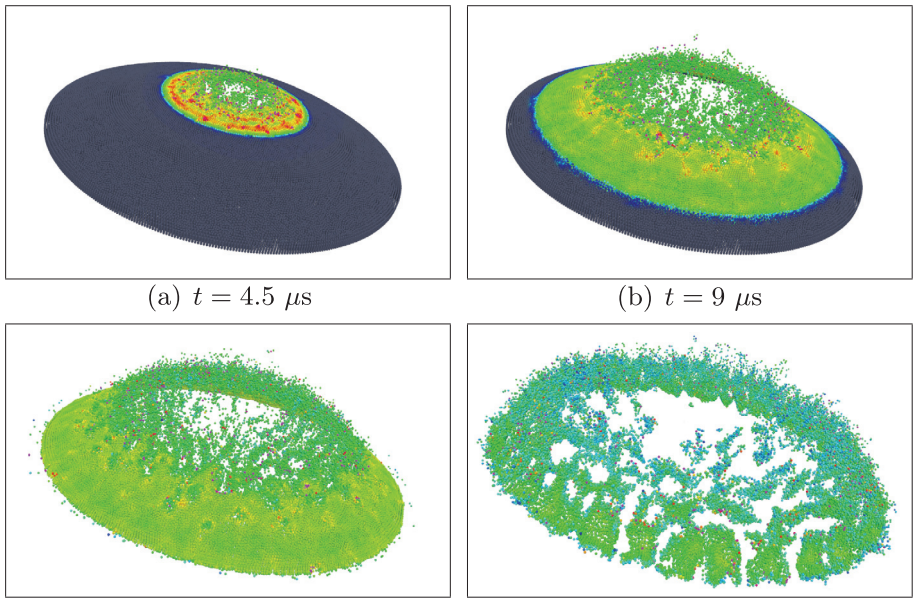

(a) $t = 4.5\ \mu$s (b) $t = 9\ \mu$s

(c) $t = 14\ \mu$s (d) $t = 25\ \mu$s

Fig. 6. Snapshots of the OTM/eigenerosion simulation of a spherical cap subjected to explosive loading. The cap is shown in nodal representation colored by von Mises stress.

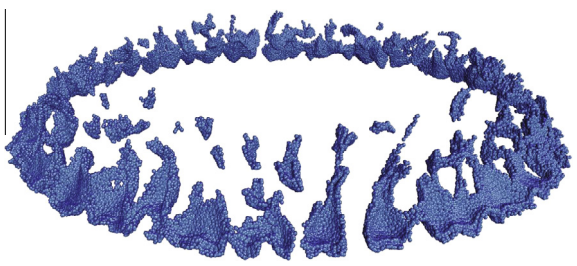

Fig. 7. The distribution of fragments at $t = 30\ \mu$s predicted by the OTM/eigenerosion simulation. The spherical cap is represented by material points.

post-mortem fragment size. The data reduction procedure adopted in the experimental paper consisted in measuring the volume and the thickness of the recovered fragments. The sizes were then evaluated as the radii of ideal disk-like fragments. We replicated the procedure by computing the volume and the thickness of the resulting fragments. In particular, we consider the uneroded material points as spheres of volume equal to their actual discrete volume. Two material points are considered to belong to the same cluster, i. e., to be connected, if their corresponding spheres overlap in space. A fragment is a cluster of connected material points. Finally, the size of each fragment is calculated by assuming an ideal disk-like shape, as described in Campbell et al. (2007). As is evident from Fig. 8, the experimental and the numerical fragment size distribution are in good agreement. In particular, the numerical mean radius 6.36 ± 2.01 mm of the fragments matches closely the corresponding experimental value of 6.95 ± 2.47 mm.

The experimental velocity of a reference spot located on the anterior surface of the spherical cap at mid-way between the center and the edge was experimentally measured by velocimetry, and the velocity history is reported in Campbell et al. (2007). This measurement enables a quantitative comparison with the simulations. To this

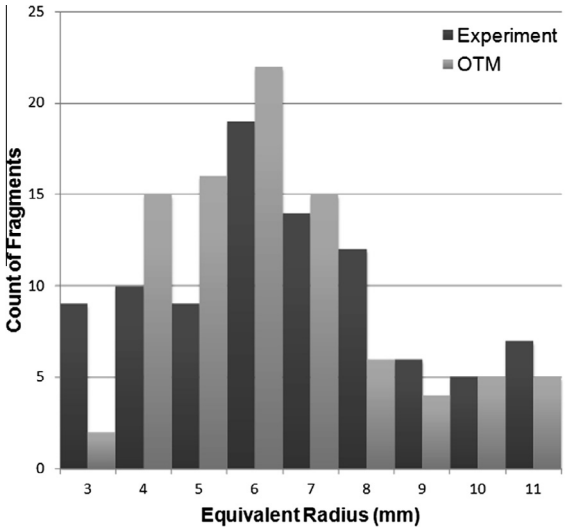

Fig. 8. Comparison of the distribution of fragment size calculated in the OTM simulation and measured in the experiment.

end, we record the linear momentum history for the set of N points located on the outer middle circumference of the shell. At each time t, the average velocity $V_{\text{mid}}(t)$ of such set of points is computed as:

$$V_{\text{mid}}(t) = \frac{\sum_{a=1}^{N} m_a(t) V_a(t)}{\sum_{a=1}^{N} m_a(t)}, \tag{14}$$

where m_a and V_a denote the mass and the velocity in the direction of the shell cap axis of the node a. Fig. 9a compares the experimental and the numerical velocities of the reference spot. The two histories are in excellent agreement during the initial stages of the test. However, whereas the final velocity of ~ 1.8 km/s is well captured by the simulations, the transient is overshot. This discrepancy may be due to a number of sources of modeling error, especially pertaining to material modeling. However, it should be carefully noted that the drive used in the simulations is highly idealized and, thus, likely a major source of error. Considering the level of uncertainty in the detonation drive, the agreement shown in Fig. 9a is quite satisfactory. A mesh convergence study is also shown in Fig. 9b for completeness. The error defined as

$$\text{Error} = \frac{|v_h - v|}{v}, \tag{15}$$

where v_h and v are the computed and exact (estimated) steady velocity and h is the mesh size. The estimated rate of convergence, $\alpha \simeq 1.58$, is indicative of better-than-linear convergence with respect to mesh size in the chosen error metric.

Campbell et al. (2007) computed the uniform strain prior to failure by measuring the thickness of the recovered fragments. Under the assumption of equi-biaxial strain on the shell surface immediately before neck formation, Campbell et al. (2007) computed the uniform strain by measuring the thickness of post-mortem fragments. Using a large number of recovered fragments, they produced the distribution of the plastic strain, characterized by mean values of 0.38 for the equi-biaxial strain and 0.76 for the through thickness strain. With the aid of images of the numerical simulation, we replicated the measurements of one representative fragment chosen between the ones generated in proximity of the edge of the spherical cap. Fig. 10 compares the final shape of the chosen fragment with the intact shell. The final thickness of the fragment as measured from the numerical results is 1.0±0.2 mm. This suggests a nominal compressive strain of 0.67±0.07 through the thickness, and a nominal uniform strain of 0.33±0.03 before necking. Such values are in good agreement with the experimental findings.

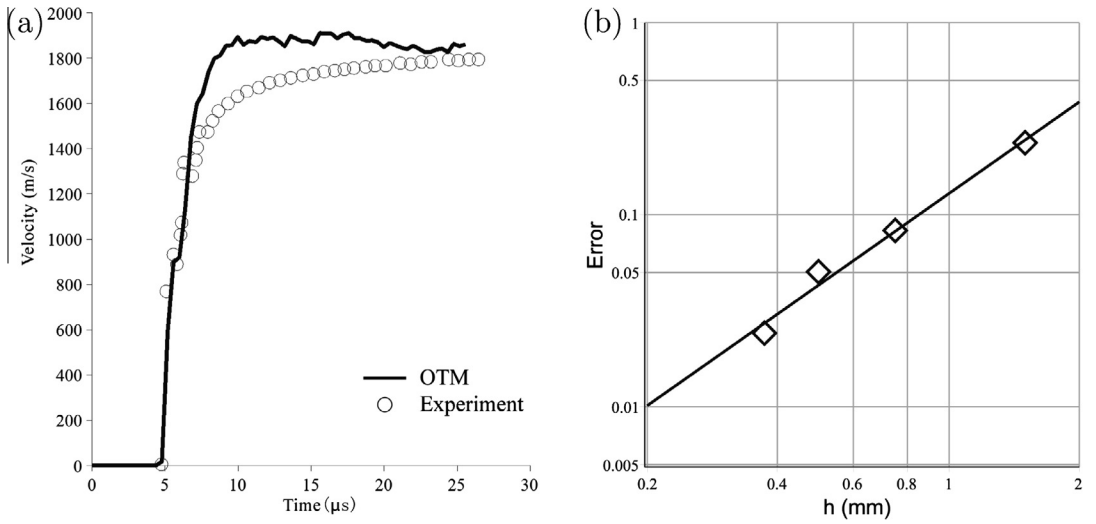

Fig. 9. (a) Comparison of the history of velocity at the midway between the pole and the edge of the shell measured in the experiment and computed with the simulations. (b) Convergence plot of the reference spot final velocity.

Fig. 10. Comparison between the original thickness of the shell (3 mm) and the thickness (1±0.2 mm) of one of the fragments resulting from the simulation.

5. Summary and concluding remarks

We have presented a validation assessment of the *eigenerosion* scheme, (Schmidt et al., 2009; Pandolfi and Ortiz, 2012; Pandolfi et al., 2013), in conjunction with the Optimal Transportation Meshfree (OTM) method, based on the detonation-driven 304L steel spherical-cap fragmentation experiments of Campbell et al. (2007). Metrics used for purposes of validation include the velocity history of a witness point of the shell and the histogram of recovered fragment sizes. The results of the simulations are found to be in overall good agreement with the experimental measurements, especially when allowances are made for the level of uncertainty arising from the characterization of the drive and material properties.

In general terms, the ability of the approach to predictively simulate exceedingly complex patterns of fracture and fragmentation under severe conditions of loading and material behavior is remarkable. This ability is all the more remarkable considering the simplicity of the approach. Indeed, in calculations the fracture behavior of the material is characterized by one single parameter, the critical energy-release rate G_c , which is amenable to direct experimental measurement, e. g., from Charpy tests or from *J*-testing (Kanninen and Popelar, 1985). In addition, it is remarkable that a simple fracture criterion, Eq. (5), in conjunction with a material-point erosion implementation, is capable of accounting for complex three-dimensional fracture processes, including mixed modes of loading, branching and fragmentation, and under diverse material conditions, including dynamic deformation, inelasticity, thermal effects, and others. From this vantage point, the power of the approach is truly extraordinary, especially when considered against the difficulties entailed in the implementation of other approaches and their limitations thereof, be them as regards material behavior, geometry, loading conditions or a combination thereof. In separate validation studies, eigenerosion has also demonstrated a high degree of accuracy and versatility in applications involving quasistatic three-dimensional crack tracking (Pandolfi et al., 2013) and brittle materials (Pandolfi and Ortiz, 2012). All these results taken together lend material-point erosion methods credence, specially provably convergent schemes such as eigenerosion, in a broad range of applications, possibly involving complex fracture and fragmentation behavior.

Acknowledgments

The authors gratefully acknowledge the support of the Department of Energy National Nuclear Security Administration under Award Number DE-FC52-08NA28613 through Caltech's ASC/PSAAP Center for the Predictive Modeling and Simulation of High Energy Density Dynamic Response of Materials.

References

Arnold, W., Rottenkolber, E., 2008. Fragment mass distribution of metal cased explosive charges. Int. J. Impact Eng. 35 (12), 1393–1398. Arroyo, M., Ortiz, M., 2006. Local maximum-entropy approximation schemes: a seamless bridge between finite elements and meshfree methods. Int. J. Numer. Methods Eng. 65, 2167–2202.

Belytschko, T., Lin, J., 1987. A three-dimensional impact-penetration algorithm with erosion. Comput. Struct. 25, 95–104.

Benamou, J.D., Brenier, Y., 1999. A numerical method for the optimal time-continuous mass transport and related problems. In: Monge-Ampère Equation: Application to Geometry and Optimization. Contemporary Mathematics, vol. 226. Americal Mathematical Society, Providence, RI, pp. 1–11.

Bentley, J.L., Friedman, J.H., 1979. Data structures for range searching. Assoc. Comput. Mach. Comput. Surv. 11, 397–409.

Borvik, T., Hopperstad, O.S., Pedersen, K.O., 2008. Quasi-brittle fracture during structural impact of AA7075-T651 aluminum plates. Int. J. Impact Eng. 37, 537–551.

Camacho, G.T., Ortiz, M., 1997. Adaptive Lagrangian modelling of ballistic penetration of metallic targets. Comput. Methods Appl. Mech. Eng. 142, 269–301.

Campbell, G.H., Archbold, G.C., Hurricane, O.A., Miller, P.L., 2007. Fragmentation in biaxial tension. J. Appl. Phys. 101, 033540.

Clifton, R.J., Klopp, R.W., 1985. Pressure-shear plate impact testing. Metals Handbook, ninth ed., vol. 8. pp. 230–239.

Drugan, W.J., 2001. Dynamic fragmentation in brittle materials: analytical mechanics-based models. J. Mech. Phys. Solids 49, 1181–1208.

Fressengeas, C., Molinari, A., 1994. Fragmentation of rapidly stretching sheets. Eur. J. Mech. A Solids 13 (2), 251–268.

Goto, D.M., Becker, R., Orzechowski, T.J., Springer, H.K., Sunwoo, A.J., Syn, C.K., 2008. Investigation of the fracture and fragmentation of explosively driven rings and cylinders. Int. J. Impact Eng. 35 (12), 1547–1556.

Grady, D.E., Kipp, M.E., Benson, D., 1984. Energy and statistical effects in the dynamic fiagmentation of metal rings. In: Harding, J. (Ed.), Mechanical Properties at High Rates of Strain. Inst. Physics, Bristol, pp. 265–322.

Guduru, P.R., Freund, L.B., 2002. The dynamics of multiple neck formation and fragmentation in ductile metals. Int. J. Solids Struct. 39, 5615–5632.

Hiroe, T., Fujiwara, K., Hata, H., Takahashi, H., 2008. Deformation and fragmentation behaviour of exploded metal cylinders and the effects of wall materials, configuration, explosive energy and initiated locations. Int. J. Impact Eng. 35 (12), 1578–1586.

Johnson, G.R., Stryk, R.A., 1987. Eroding interface and improved tetrahedral element algorithms for high velocity impacts in three dimensions. Int. J. Impact Eng. 5, 414–427.

Johnson, G.R., Stryk, R.A., 1990. User instruction for the 1990 version of the combined (1D, 2D, 3D) EPIC code. Technical Report DE-AC04-87AL-42550, DARPA, 1990.

Jordan, R., 1998. The variational formulation of the Fokker-Planck equation. SIAM J. Math. Anal. 29, 1–17.

Kane, C., Marsden, J.E., Ortiz, M., 1999. Symplectic-energy-momentum preserving variational integrators. J. Math. Phys. 40, 3353–3371.

Kanninen, M.F., Popelar, C.H., 1985. Fracture Mechanics. Oxford University Press, New York.

Kinney, G.F., 1962. Explosive Shocks in Air. The MacMillan Company, New York.

Kipp, M.E., Grady, D.E., 1986. Random flaw nucleation and interaction in one dimension. In: Mum, L.E., Staudhammer, K.P., Meyers, M.A. (Eds.), Metallurgical Applications of Shock-Wave and High-Strain-Rate Phenomena. Marcel Dekker Inc.

Klopp, R.W., Clifton, R.J., Shawki, T.G., 1985. Pressure-shear impact and the dynamic viscoplastic response of metals. Mech. Mater. 4, 375–385.
Lemonds, J., Needleman, A., 1986. Finite element analysis of shear localization in rate and temperature dependent solids. Mech. Mater. 5, 339–361.
Li, S., Qian, D., Liu, W.K., Belytschko, T., 2001. A meshfree contact-detection algorithm. Comput. Methods Appl. Mech. Eng. 190, 3271–3292.
Li, B., Habbal, F., Ortiz, M., 2010. Optimal transportation meshfree approximations schemes for fluid and plastic flows. Int. J. Numer. Methods Eng. 83 (12), 1541–1579.
Li, B., Kadane, A., Ravichandran, G., Ortiz, M., 2012. Verification and validation of the optimal-transportation meshfree (OTM) simulation of terminal ballistics. Int. J. Impact Eng. 42, 25–36.
Marusich, T.D., Ortiz, M., 1995. Modelling and simulation of high-speed machining. Int. J. Numer. Methods Eng. 38, 3675–3694.
Miller, O., Freund, L.B., Needleman, A., 1999. Modeling and simulation of dynamic fragmentation in brittle materials. Int. J. Fract. 96 (2), 101–125.
Mott, N.F., 1947. Fragmentation of shell cases. Proc. R. Soc. London A 2, 300–308.
Negri, M., 2003. Finite element approximation of the Griffith's model in fracture mechanics. Numer. Math. 95 (4), 653–687.
Ortiz, M., Giannakopoulos, A.E., 1990. Crack propagation in monolithic ceramics under mixed mode loading. Int. J. Fract. 44, 233–258.
Ortiz, M., Pandolfi, A., 2004. A variational Cam-clay theory of plasticity. Comput. Methods Appl. Mech. Eng. 193, 2645–2666.
Ortiz, M., Stainier, L., 1999. The variational formulation of viscoplastic constitutive updates. Comput. Methods Appl. Mech. Eng. 171, 419–444.
Pandolfi, A., Ortiz, M., 2012. An eigenerosion approach to brittle fracture. Int. J. Numer. Methods Eng. 92 (8), 694–714.
Pandolfi, A., Krysl, P., Ortiz, M., 1999. Finite element simulation of ring expansion and fragmentation: the capturing of length and time scales through cohesive models of fracture. Int. J. Fract. 95, 279–397. Pandolfi, A., Li, B., Ortiz, M., 2013. Modeling fracture by material-point erosion. Int. J. Fract., online first:– 2013.
Repetto, E.A., Radovitzky, R., Ortiz, M., 2000. Finite element simulations of dynamic fracture and fragmentation of glass rods. Comput. Methods Appl. Mech. Eng. 183, 3–14.
Schmidt, B., Fraternali, F., Ortiz, M., 2009. Eigenfracture: an eigendeformation approach to variational fracture. SIAM J. Multiscale Model. Simul. 7, 1237–1266.
Shenoy, V.B., 2003. Multi-scale modeling strategies in materials science–the quasicontinuum method. Bull. Mater. Sci. 26, 53–62.
Sulsky, D., Chen, Z., Schreyer, H.L., 1994. A particle method for history-dependent materials. Comput. Methods Appl. Mech. Eng. 118, 179–196.
Tong, W., Clifton, R.J., Huang, S., 1992. Pressure-shear impact investigation of strain rate history effects in oxygen-free high-conductivity copper. J. Mech. Phys. Solids 40, 1251–1294.
Villani, C., 2003. Topics in optimal transportation theory. Graduate Studies in Mathematics, vol. 58. American Mathematical Sociey, Providence, RI.
Whirley, R.G., Hallquist, J.O., 1991. DYNA-3D User manual. Technical Report Technical Report UCRL-MA-107254, Lawrence Livermore National Laboratory, 1991.
Yadav, S., Repetto, E.A., Ravichandran, G., Ortiz, M., 2001. A computational study of the influence of thermal softening on ballistic penetration in metals. Int. J. Impact Eng. 25 (8), 787–803.
Zhang, Y.Y., Chen, L., 2009. Impact simulation using simplified meshless method. Int. J. Impact Eng. 36, 651–658.
Zhou, F., Molinari, J.-F., Ramesh, K.T., 2005. A cohesive model based fragmentation analysis: effects of strain rate and initial defects distribution. Int. J. Solids Struct. 42, 5181–5207.